ICES REPORT 11-28

September 2011

Isogeometric Variational Multiscale Large-Eddy Simulation of Fully-developed Turbulent Flow over a Wavy Wall

by

K. Chang, T.J.R. Hughes, and V.M. Calo

The Institute for Computational Engineering and Sciences
The University of Texas at Austin
Austin, Texas 78712

Reference: K. Chang, T.J.R. Hughes, and V.M. Calo, "Isogeometric Variational Multiscale Large-Eddy Simulation of Fully-developed Turbulent Flow over a Wavy Wall", ICES REPORT 11-28, The Institute for Computational Engineering and Sciences, The University of Texas at Austin, September 2011.

Report Documentation Page

Form Approved
OMB No. 0704-0188

1. REPORT DATE	2. REPORT TYPE	3. DATES COVERED
SEP 2011		**00-00-2011 to 00-00-2011**

4. TITLE AND SUBTITLE	5a. CONTRACT NUMBER
Isogeometric Variational Multiscale Large-Eddy Simulation of Fully-developed Turbulent Flow over a Wavy Wall	5b. GRANT NUMBER
	5c. PROGRAM ELEMENT NUMBER
6. AUTHOR(S)	5d. PROJECT NUMBER
	5e. TASK NUMBER
	5f. WORK UNIT NUMBER
7. PERFORMING ORGANIZATION NAME(S) AND ADDRESS(ES) **University of Texas at Austin,Institute for Computational Engineering and Sciences,Austin,TX,78712**	8. PERFORMING ORGANIZATION REPORT NUMBER
9. SPONSORING/MONITORING AGENCY NAME(S) AND ADDRESS(ES)	10. SPONSOR/MONITOR'S ACRONYM(S)
	11. SPONSOR/MONITOR'S REPORT NUMBER(S)

12. DISTRIBUTION/AVAILABILITY STATEMENT
Approved for public release; distribution unlimited

13. SUPPLEMENTARY NOTES

14. ABSTRACT

We report on the isogeometric residual-based variational multiscale (VMS) Large Eddy Simulation of a fully developed turbulent flow over a wavy wall. To assess the predictive capability of the VMS modeling framework, we compare its predictions against the results from direct numerical simulation (DNS) and, when available against experimental measurements. We use C1 quadratic B-spline basis functions to represent the smooth geometry of the sinusoidal lower wall and the solution variables. The Reynolds number of the flow considered is 6,760 based on the bulk velocity and average channel height. The ratio of amplitude to wavelength (α/λ) of the sinusoidal wavy surface is set to 0.05. The computational domain is 2λ?.05λ?#955; in the streamwise, wall-normal and spanwise directions, respectively. Mean averaged quantities, including velocity and pressure profiles, and the separation/reattachment points in the recirculation region, are compared with DNS and experimental data. The turbulent kinetic energy and Reynolds stress are in good agreement with benchmark data. Coherent structures over the wavy wall are observed in isosurfaces of the Qcriterion and show similar features to those previously reported in the literature. Comparable accuracy to DNS solutions is obtained with at least one order of magnitude fewer degrees of freedom.

15. SUBJECT TERMS

16. SECURITY CLASSIFICATION OF:			17. LIMITATION OF ABSTRACT	18. NUMBER OF PAGES	19a. NAME OF RESPONSIBLE PERSON
a. REPORT	b. ABSTRACT	c. THIS PAGE			
unclassified	**unclassified**	**unclassified**	**Same as Report (SAR)**	**21**	

Isogeometric Variational Multiscale Large-Eddy Simulation of Fully-developed Turbulent Flow over a Wavy Wall

K. Chang[1], T.J.R. Hughes[2], and V.M. Calo[3]
[1]Aeromechanical Engineering, Hanseo University,
San 105, Taean, South Korea
[2]Institute for Computational Engineering and Sciences (ICES),
The University of Texas at Austin, Austin, TX 78712, USA
[3]Applied Mathematics & Computing Science and Earth Science & Engineering
King Abdullah University of Science and Technology (KAUST)
Thuwal 23955-6900, Kingdom of Saudi Arabia

Abstract

We report on the isogeometric residual-based variational multiscale (VMS) Large Eddy Simulation of a fully developed turbulent flow over a wavy wall. To assess the predictive capability of the VMS modeling framework, we compare its predictions against the results from direct numerical simulation (DNS) and, when available, against experimental measurements. We use C^1 quadratic B-spline basis functions to represent the smooth geometry of the sinusoidal lower wall and the solution variables. The Reynolds number of the flow considered is 6,760 based on the bulk velocity and average channel height. The ratio of amplitude to wavelength (α/λ) of the sinusoidal wavy surface is set to 0.05. The computational domain is $2\lambda \times 1.05\lambda \times \lambda$ in the streamwise, wall-normal and spanwise directions, respectively. Mean averaged quantities, including velocity and pressure profiles, and the separation/reattachment points in the recirculation region, are compared with DNS and experimental data. The turbulent kinetic energy and Reynolds stress are in good agreement with benchmark data. Coherent structures over the wavy wall are observed in isosurfaces of the Q-criterion and show similar features to those previously reported in the literature. Comparable accuracy to DNS solutions is obtained with at least one order of magnitude fewer degrees of freedom.

Keywords: Variational multiscale modeling, Large Eddy Simulation, Wavy wall, Isogeometric analysis, B-spline finite elements

1. Introduction

Fully developed turbulent flows over wavy surfaces are relevant for many engineering applications, such as, pipe flow in a heat exchanger where wall waviness enhances heat transfer and gas-liquid contractors in the chemical industry. The wavy wall induces the alternation of favorable and adverse pressure gradients and a large ratio of amplitude to wavelength (α/λ) generates a complex recirculating flow, which enhances turbulent mixing.

Many experimental and numerical studies have been conducted to understand the complex physics of fully developed turbulent flows over wavy walls. Hudson et al. [1] measured the spatial and temporal variation of the velocity components in a flow

with wavy walls using Laser Doppler Velocimetry (LDV) and reported mean velocity fields and fluctuating quantities such as turbulent stresses and kinetic-energy production. In their experiment, the Reynolds number based on bulk velocity and channel height is 6,760 and the amplitude to wavelength ratio is equal to 0.05. These measurements are used to benchmark our simulations. The experiments showed that the shear layer in the vicinity of the separation region is the locus of large turbulent kinetic energy production and Reynolds stresses.

Günther and Rohr [2] studied streamwise structures and the three-dimensional flow field using proper orthogonal decomposition (POD) in their particle image velocimetry (PIV) experiment. They identified the characteristic length-scale of the longitudinal structures as 1.5λ in both laminar and turbulent wavy wall flows and POD results revealed smaller structures at the maximum Reynolds stress location.

Maass and Schumann [3] performed direct numerical simulation (DNS) of turbulent wavy wall flows using the finite difference method and showed the effective friction velocity is about 50% larger at the wavy surface than at the flat surface because of the additional pressure drag.

Cherukat et al. [4] conducted DNS studies of the turbulent flow over a sinusoidal wavy surface using spectral elements of 7th order. Their results were validated with the experimental data of Hudson et al. [1] and are considered a reliable benchmark for numerical simulation of wavy walls. They report instantaneous flow fields and turbulent statistics and used them to find velocity bursts in the separated-flow region that extend over large distances away from the wall.

Recently, Yoon et al. [5] investigated the effect of wave amplitude on turbulent flow in a wavy channel using DNS with the immersed boundary method. They observed that the pressure drag coefficient increases as the ratio α/λ increases, whereas the friction drag coefficient is maximum at the specified amplitude to wavelength ratio, α/λ=0.3.

In [6], Park et al. compared several Reynolds-Averaged Navier Stokes (RANS) models, such as standard k-ε and linear/nonlinear k-ε-f_μ and showed that most RANS models tested have severe limitations in predicting flow separation appropriately with the exception of the nonlinear k-ε-f_μ model. The nonlinear k-ε-f_μ model shows good agreement with DNS results in mean flow field, streamwise fluctuations, and Reynolds stresses, however, it exhibits discrepancies in other turbulent quantities such as wall-normal fluctuations.

Most of the previous numerical simulations of the fully developed turbulent flow over a wavy wall have been done using DNS to capture the separated flow field and to collect turbulent statistics. However, very fine resolutions are required to resolve the Kolmogorov length scale of the boundary layer, which implies a large computational burden. To overcome these difficulties, we believe that Large Eddy Simulation (LES) is an adequate tool, since separation and turbulence fluctuations can be captured well while utilizing significantly less computational resources.

The recently proposed Variational Multiscale Method [7,8] has proven to be an

effective approach to LES and yields new insights into classical LES challenges such as scale separation and closure modeling. The proposed residual-based variational multiscale (VMS) framework uses analytical tools to approximate the effect of the fine scales in the coarse-scale governing equations, such as, perturbation series arguments and the fine-scale Green's function; see e.g. [7]. In this framework, the simplest approximation to the fine scales is given in the form of a scaled residual of the coarse scales. This VMS methodology was validated in bypass transition [9], forced isotropic turbulence and fully-developed channel flows [7,10], on free-surface [11], Taylor-Couette flows [12], and, in conjunction with the weak imposition of Dirichlet boundary conditions, in high Reynolds number channel and asymmetric diffuser flows [13].

In this study, we further validate isogeometric VMS methodology in a turbulent flow with separation, that is, in fully-developed turbulent flow over a wavy wall. We report mean fields and turbulent statistics of the flow such as Reynolds stress, kinetic energy and production. Additionally, instantaneous velocity fields are studied and their coherent structures described.

The organization of the paper is as follows. In Section 2, following [7], we briefly summarize the residual-based variational multiscale formulation for the incompressible Navier-Stokes equations and introduce the numerical procedure used to discretize the resulting non-linear system of equations. In Section 3, we present the problem setup describing the computational domain, boundary conditions and meshes used. In Section 4, we present the main results for the wavy wall simulations and compare these with DNS results and experimental data. In section 5 we draw conclusions.

2. Residual based Variational Multiscale Method

The incompressible Navier-Stokes equations are:

$$\frac{\partial \boldsymbol{u}}{\partial t} + \nabla \cdot (\boldsymbol{u} \otimes \boldsymbol{u}) + \nabla p = \nu \Delta \boldsymbol{u} + \boldsymbol{f} \quad \text{in } \Omega \tag{1}$$

$$\nabla \cdot \boldsymbol{u} = 0 \quad \text{in } \Omega \tag{2}$$

$$\boldsymbol{u}(0^+) = \boldsymbol{u}(0^-) \quad \text{in } \Omega \tag{3}$$

$$\boldsymbol{u} = 0 \quad \text{on } \Gamma \tag{4}$$

where $\boldsymbol{u}$ is the flow velocity, p is the pressure, $\boldsymbol{f}:\Omega \rightarrow \mathrm{R}^3$ is a given body force, ν is the kinematic viscosity, and the symbol, $\otimes$ denotes the tensor product. Equations (1) and (2) represent the balance of linear momentum and mass, respectively, while equations (3) and (4) describe the initial and boundary conditions, where $\boldsymbol{u}_0$ is the given initial velocity distribution. Let $\boldsymbol{V}$ denote both the trial solution and weighting function spaces, which are assumed to be identical. The variational formulation can be expressed as follows:

Find $\boldsymbol{U} \in \boldsymbol{V}$ such that $\forall \boldsymbol{W} \in \boldsymbol{V}$:

$$B(\boldsymbol{W}, \boldsymbol{U}) = B_1(\boldsymbol{W}, \boldsymbol{U}) + B_2(\boldsymbol{W}, \boldsymbol{U}, \boldsymbol{U}) = L(\boldsymbol{W}) \tag{5}$$

with

$$B_1(\boldsymbol{W},\boldsymbol{U}) = \left(\boldsymbol{w}, \frac{\partial \boldsymbol{u}}{\partial t}\right)_\Omega + (q, \nabla \cdot \boldsymbol{u})_\Omega - (\nabla \cdot \boldsymbol{w}, p)_\Omega + (\nabla^s \boldsymbol{w}, 2\nu \nabla^s \boldsymbol{u})_\Omega \tag{6}$$

$$B_2(\boldsymbol{W},\boldsymbol{U},\boldsymbol{V}) = -(\nabla \boldsymbol{w}, \boldsymbol{u} \otimes \boldsymbol{v})_\Omega \tag{7}$$

$$L(\boldsymbol{W}) = (\boldsymbol{w}, \boldsymbol{f})_\Omega \tag{8}$$

where $\boldsymbol{U}=\{\boldsymbol{u}, p\}$ and $\boldsymbol{W}=\{\boldsymbol{w},q\}$ belong to $\boldsymbol{V}$. $B_1(\cdot,\cdot)$ is a bilinear form and $B_2(\cdot,\cdot,\cdot)$ is a trilinear form.

The solution and weighting function spaces are decomposed into coarse-scale and fine-scale subspaces as follows:

$$\boldsymbol{V} = \overline{\boldsymbol{V}} \oplus \boldsymbol{V}' \tag{9}$$

where $\overline{\boldsymbol{V}}$ is the finite-dimensional space associated with the coarse scales of the problem and $\boldsymbol{V}'$ is the complement of $\overline{\boldsymbol{V}}$ in $\boldsymbol{V}$ and is associated with fine-scale variables. We indentify $\overline{\boldsymbol{V}}$ with the numerical solution of the resulting discrete variational system. Using the linearity of [5] with respect to the weighting functions, we divide the variational system into a coupled coarse-scale and fine-scale equation system:

$$B(\overline{\boldsymbol{W}}, \overline{\boldsymbol{U}} + \boldsymbol{U}') = L(\overline{\boldsymbol{W}}), \quad \forall \overline{\boldsymbol{W}} \in \overline{\boldsymbol{V}} \tag{10}$$

$$B(\boldsymbol{W}', \overline{\boldsymbol{U}} + \boldsymbol{U}') = L(\boldsymbol{W}'), \quad \forall \boldsymbol{W}' \in \boldsymbol{V}' \tag{11}$$

where $\overline{\boldsymbol{U}} \in \overline{\boldsymbol{V}},\ \boldsymbol{U}' \in \boldsymbol{V}'$

$$\begin{aligned} B(\overline{\boldsymbol{W}}, \overline{\boldsymbol{U}} + \boldsymbol{U}') = {} & B_1(\overline{\boldsymbol{W}}, \overline{\boldsymbol{U}}) + B_1(\overline{\boldsymbol{W}}, \boldsymbol{U}') + B_2(\overline{\boldsymbol{W}}, \overline{\boldsymbol{U}}, \overline{\boldsymbol{U}}) + B_2(\overline{\boldsymbol{W}}, \overline{\boldsymbol{U}}, \boldsymbol{U}') \\ & + B_2(\overline{\boldsymbol{W}}, \boldsymbol{U}', \overline{\boldsymbol{U}}) + B_2(\overline{\boldsymbol{W}}, \boldsymbol{U}', \boldsymbol{U}') \end{aligned} \tag{12}$$

$$\begin{aligned} B(\boldsymbol{W}', \overline{\boldsymbol{U}} + \boldsymbol{U}') = {} & B_1(\boldsymbol{W}', \overline{\boldsymbol{U}}) + B_1(\boldsymbol{W}', \boldsymbol{U}') + B_2(\boldsymbol{W}', \overline{\boldsymbol{U}}, \overline{\boldsymbol{U}}) + B_2(\boldsymbol{W}', \overline{\boldsymbol{U}}, \boldsymbol{U}') \\ & + B_2(\boldsymbol{W}', \boldsymbol{U}', \overline{\boldsymbol{U}}) + B_2(\boldsymbol{W}', \boldsymbol{U}', \boldsymbol{U}') \end{aligned} \tag{13}$$

Using integration by parts, we rearrange equation (13) as:

$$B_{\overline{U}}(\boldsymbol{W}', \boldsymbol{U}') + B_2(\boldsymbol{W}', \boldsymbol{U}', \boldsymbol{U}') = \left\langle \boldsymbol{W}', \mathrm{Res}(\overline{\boldsymbol{U}}) \right\rangle_{V', V'^*} \tag{14}$$

where

$$B_{\overline{U}}(\boldsymbol{W}', \boldsymbol{U}') = B_1(\boldsymbol{W}', \boldsymbol{U}') + B_2(\boldsymbol{W}', \boldsymbol{U}', \overline{\boldsymbol{U}}) + B_2(\boldsymbol{W}', \overline{\boldsymbol{U}}, \boldsymbol{U}') \tag{15}$$

$$\left\langle \boldsymbol{W}', \mathrm{Res}(\overline{\boldsymbol{U}}) \right\rangle_{V', V'^*} = L(\boldsymbol{W}') - B_1(\boldsymbol{W}', \overline{\boldsymbol{U}}) + B_2(\boldsymbol{W}', \overline{\boldsymbol{U}}, \overline{\boldsymbol{U}}) \tag{16}$$

$\mathrm{Res}(\overline{\boldsymbol{U}})$ represents the residual of coarse-scales and $\langle \cdot, \cdot \rangle_{V', V'^*}$ is the duality pairing between $\boldsymbol{V}'$ and $\boldsymbol{V}'^*$. Thus, we think of $\boldsymbol{U}'$ as the solution of the non-linear problem described by (14). It is abstractly expressed as a function of $\overline{\boldsymbol{U}}$ and $\mathrm{Res}(\overline{\boldsymbol{U}})$ as follows:

$$\boldsymbol{U}' = \boldsymbol{F}'\left(\overline{\boldsymbol{U}}, \mathrm{Res}(\overline{\boldsymbol{U}})\right)$$

(17)

Following [7], once we introduce a disctretization and indentify the coarse scales with the resolved scales, $\boldsymbol{U}^h$, we approximate the fine-scale Green's operator, which arises in the perturbation series solution of (15), with an element-wise stabilization operator $\boldsymbol{\tau}$ and residual of the coarse scales $\mathrm{Res}(\boldsymbol{U}^h)$ as follows:

$$\widetilde{\boldsymbol{U}}' \approx -\boldsymbol{\tau}\mathrm{Res}(\widetilde{\boldsymbol{U}}^h) \tag{18}$$

These approximate fine scales are expressed in terms of the resolved velocity and pressure fields as

$$\widetilde{\boldsymbol{U}}' = \begin{Bmatrix} \tilde{\boldsymbol{u}}' \\ \tilde{p}' \end{Bmatrix} = \begin{Bmatrix} -\tau_M \boldsymbol{r}_M(\boldsymbol{u}^h, p^h) \\ -\tau_C r_C(\boldsymbol{u}^h) \end{Bmatrix} \tag{19}$$

where r_M and r_C are the coarse-scale residuals of the momentum and continuity equations, respectively. The scaling factors, also known as intrinsic times, τ_M and τ_C, are element-wise stabilization parameters for the momentum and continuity equations. The residuals and scaling factors are defined below:

$$\begin{aligned}
r_M(\boldsymbol{u}^h, p^h) &= \frac{\partial \boldsymbol{u}^h}{\partial t} + \boldsymbol{u}^h \cdot \nabla \boldsymbol{u}^h + \nabla p^h - \nu \Delta \boldsymbol{u}^h - f \\
r_C(\boldsymbol{u}^h) &= \nabla \cdot \boldsymbol{u}^h \\
\tau_M &= \left(\frac{4}{\Delta t^2} + \boldsymbol{u}^h \cdot \boldsymbol{G} \boldsymbol{u}^h + C_I v^2 \boldsymbol{G} : \boldsymbol{G} \right)^{-1/2} \\
\tau_C &= (\tau_M \boldsymbol{g} \cdot \boldsymbol{g})^{-1} \\
G_{ij} &= \sum_{k=1}^{3} \frac{\partial \xi_k}{\partial x_i} \frac{\partial \xi_k}{\partial x_j} \\
g_i &= \sum_{j=1}^{3} \frac{\partial \xi_j}{\partial x_i}.
\end{aligned} \tag{20}$$

where x_i is a physical-space coordinate and ξ_i is a parameter-space coordinate (i.e., reference element coordinate). C_I is set to 36 through derivation of an inverse estimate [7]. Finally, the formulation of the residual-based variational multiscale method reads as follows:

Find $\boldsymbol{U}^h$ such that $\forall \boldsymbol{W}^h$:

$$B^{MS}(\boldsymbol{W}^h, \boldsymbol{U}^h) - L^{MS}(\boldsymbol{W}^h) = 0 \tag{21}$$

$$\begin{aligned}
B^{MS}(\boldsymbol{W}^h, \boldsymbol{U}^h) = {} & B^G(\boldsymbol{W}^h, \boldsymbol{U}^h) \\
& + (\boldsymbol{u}^h \cdot \nabla \boldsymbol{w}^h + \nabla q^h, \tau_M \boldsymbol{r}_M(\boldsymbol{u}^h, p^h))_\Omega + (\nabla \cdot \boldsymbol{w}^h, \tau_C r_C(\boldsymbol{u}^h))_\Omega \\
& + (\boldsymbol{u}^h \cdot (\nabla \boldsymbol{w}^h)^T, \tau_M \boldsymbol{r}_M(\boldsymbol{u}^h, p^h))_\Omega - (\nabla \boldsymbol{w}^h, \tau_M \boldsymbol{r}_M(\boldsymbol{u}^h, p^h) \otimes \tau_M \boldsymbol{r}_M(\boldsymbol{u}^h, p^h))_\Omega
\end{aligned} \tag{22}$$

$$L^{MS}(\boldsymbol{W}^h) = (\boldsymbol{w}^h, \boldsymbol{f})_\Omega \tag{23}$$

$$B^G(\boldsymbol{W}^h, \boldsymbol{U}^h) = \left(\boldsymbol{w}^h, \frac{\partial \boldsymbol{u}^h}{\partial t}\right)_\Omega - \left(\nabla \boldsymbol{w}^h, \boldsymbol{u}^h \otimes \boldsymbol{u}^h\right)_\Omega - (\nabla \cdot \boldsymbol{w}^h, p^h)_\Omega + (\nabla^s \boldsymbol{w}^h, 2\nu \nabla^s \boldsymbol{u}^h)_\Omega + (q^h, \nabla \cdot \boldsymbol{u}^h)_\Omega \tag{24}$$

where the superscripts *G* and *MS* stand for Galerkin and variational multiscale, respectively.

We use the generalized-α method as presented by Jansen et al. [14] to integrate the governing equations in time. We set ρ_∞=0.5, where ρ_∞ is the spectral radius of the amplification matrix as $\Delta t \to \infty$. To solve the nonlinear system of equations, we employ Newton's method with a two-stage predictor-multicorrector algorithm. See [7] for further details.

3. Numerical simulation

The Reynolds number is 6,760 based on the bulk velocity and average channel height. The geometry of the wavy wall is described by the formula $\alpha\cos(2\pi x/\lambda)$, where α is the amplitude of the wave and λ is the wavelength. Herein, the ratio (α/λ) of the amplitude to the wavelength is set to 0.05, which is the same as that in references [3-5].

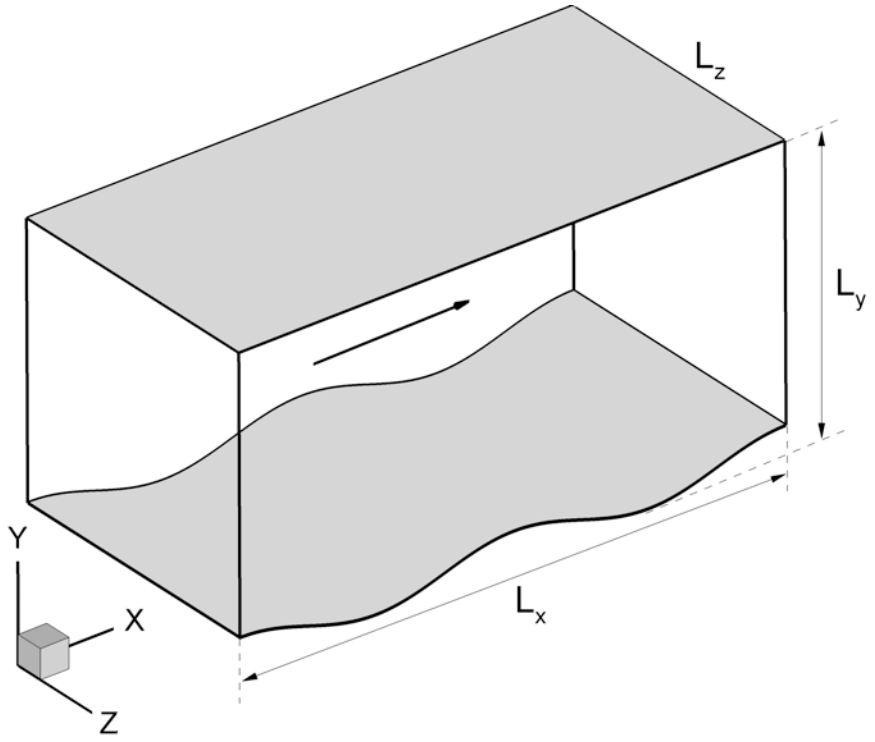

Figure 1. Computational domain.

The computational domain ($L_x \times L_y \times L_z$) shown in Figure 1 has dimensions of $2\lambda \times 1.05\lambda \times \lambda$ in the streamwise (x), vertical (y) and spanwise (z) directions. This is identical to the one used by Yoon et al. [5]. We employ no-slip Dirichlet boundary

conditions at the lower wavy wall and at the upper flat wall (y=1.0λ), and we apply periodic boundary conditions in both the streamwise and spanwise directions. The driving force is the streamwise pressure gradient which is adjusted to maintain a constant mass flow rate.

Isogeometric analysis [15] with B-spline basis functions is employed in the present work. The control points for the B-spline curve defining the geometry are obtained by projecting the known sinusoidal geometry onto the coarsest possible quadratic B-spline space that can represent the geometry [16, 17]. The open, non-uniform knot vector is:

$$\Xi = \{0,0,0,1,2,3,4,5,6,7,8,8,8\}$$

and the control points are reported in Table 1.

Table 1. Control points for the B-spline curve defining the bottom wavy wall.

	x	y
B_1	0.0000E+00	5.0000E-02
B_2	3.1250E-02	4.9998E-02
B_3	9.3750E-02	4.2370E-02
B_4	1.5625E-01	2.8299E-02
B_5	2.1875E-01	9.9351E-03
B_6	2.8125E-01	-9.9350E-03
B_7	3.4375E-01	-2.8299E-02
B_8	4.0625E-01	-4.2370E-02
B_9	4.6875E-01	-4.9998E-02
B_{10}	5.0000E-01	-5.0000E-02

4. Results: Simulation of wavy wall channel flows

We analyzed the sensitivity of the simulation results to the grid resolution using the following three cases: 128×64×64 (Fine mesh), 64×32×32 (Medium mesh) and 32×16×16 (Coarse mesh). The resolutions correspond to the streamwise, vertical and spanwise directions, respectively. For all meshes, C^1-continuous quadratic B-splines basis functions are used. The geometry definition and solution variables use identical parameterization (isoparametric disctretization). The number of mesh elements for the three cases is summarized and compared with meshes used in other DNS computations in Table 2. An equivalent number of mesh points per unit streamwise and unit spanwise wave length are reported in Table 2 to allow a fair comparison of the different simulations, since different computational domain sizes were used in each simulation. As mentioned previously, the spectral element method of Cherukat el al. [4] employs 7th order Lagrange polynomials. The total number of mesh points is 64×148×32, which is greater than 3.0×10^5. In the other two DNS cases, based on finite difference and finite volume methods, 3.0×10^5 and 1.8×10^6 mesh points are used. The number of degrees of freedoms in the medium mesh case of the present work is 3.3×10^4 ($=32^3$), which is at least an order of magnitude fewer than those used in the DNS calculations.

Table 2. Mesh elements in the present work and in the DNS calculations of others.

	L_x	L_y	L_z	N_x	N_y	N_z	N_x/λ	N_z/λ
Coarse (present)	2λ	1.05λ	λ	32	16	16	16	16
Medium (present)				64	32	32	32	32
Fine (present)				128	64	64	64	64
Cherukat et al. [4]*	4λ	1.05λ	2λ	36	21	64	9	32
Maass and Schumann [3]	4λ	1.05λ	2λ	256	128	96	64	48
Yoon et al. [5]	2λ	1.05λ	λ	250	150	100	125	100

* Spectral method with 7th order Lagrange polynomials.

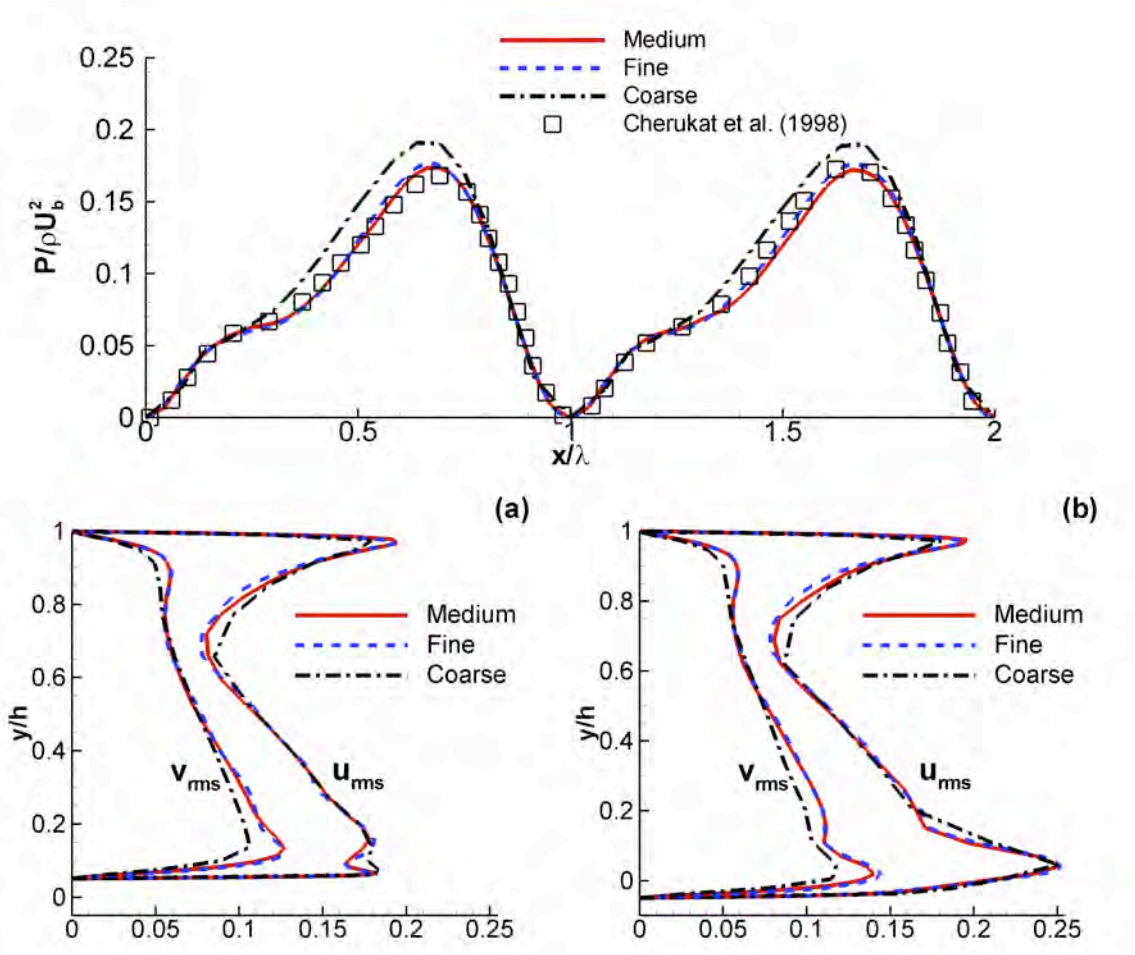

Figure 2. Grid convergence test, top: pressure coefficient distribution at the wall, bottom: u_{rms}, v_{rms} at two positions (a) x/λ=0.0 (crest), (b) x/λ=0.5 (trough).

Results for the three meshes are presented in Figure 2. The mean pressure coefficient at the wavy wall shows that the coarse-mesh result has small discrepancies compared with the two finer cases. The root-mean-square (rms) velocity fluctuations are compared in Figure 2 at two positions: the crest (x/λ=0.0) and the trough (x/λ=0.5). Velocity fluctuations of the medium and fine meshes are consistent with each other, while the coarse mesh fails to properly resolve the velocity fluctuations. This lack of resolution is particularly noticeable in the region of rapid variation near the peak. Based on these results, the medium mesh (64×32×32) is considered to be adequate.

To compute the mean flow quantities, we averaged the instantaneous velocity and pressure fields in the spanwise direction and in time over a period of $100H/U_b$, where H is the channel height and U_b is the mean bulk velocity.

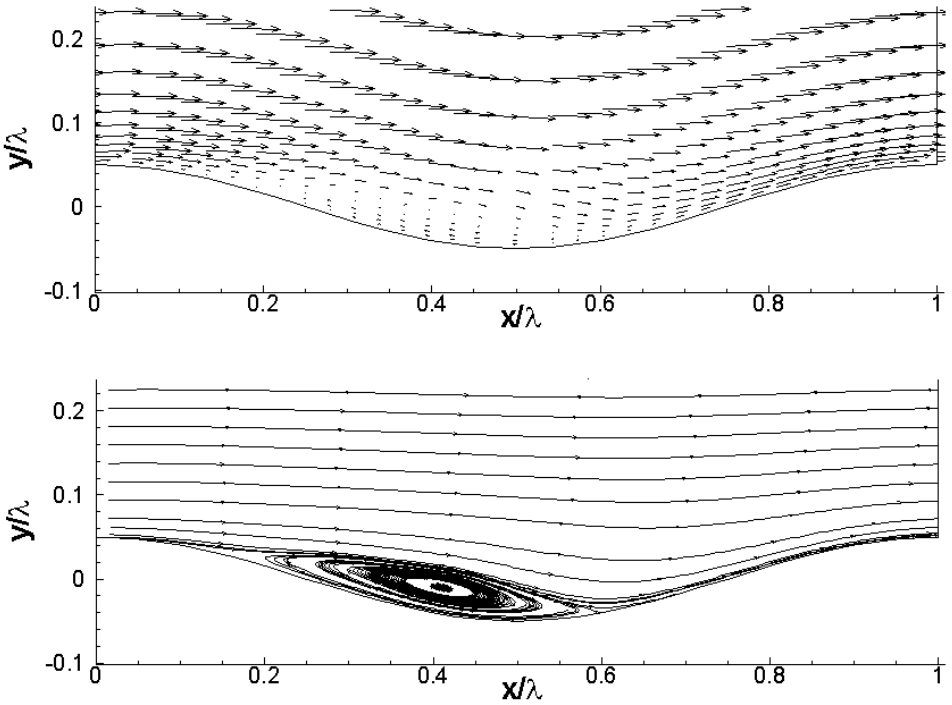

Figure 3. Top: mean velocity vectors; bottom: mean streamlines (medium mesh case).

Figure 3 shows mean velocity vectors and streamlines for the medium mesh case. It can be seen that the turbulent boundary layer near the wall is well resolved.

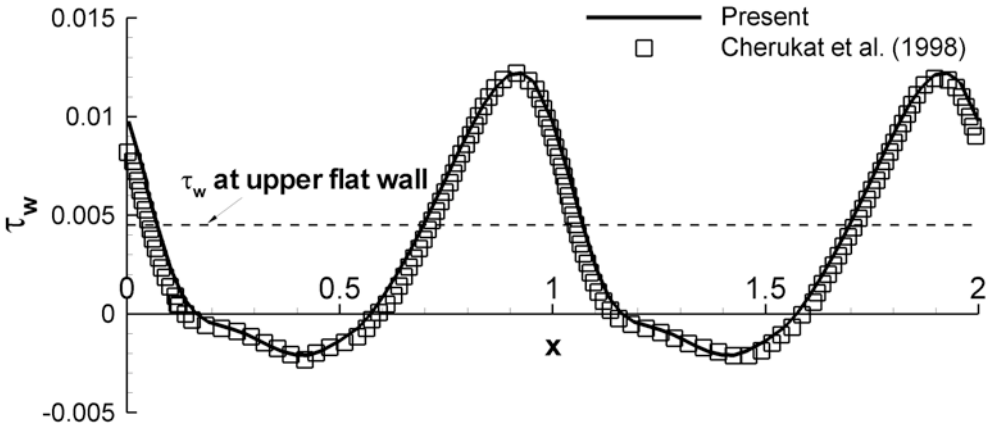

Figure 4. Shear stress at the wall (medium mesh case).

To determine the separation and reattachment points, the wall shear stress is calculated

and shown in Figure 4. The separation point is seen to be predicted at x/λ=0.15 and the reattachment point at x/λ=0.58. The DNS results of Cherukat et al. [4] give the corresponding points at 0.14 and 0.59, and the experiment of Hudson et al. [1] determined these points as 0.22 and 0.58. As argued by Cherukat et al. [4], this difference in the measured separation point between numerical simulation and experiment may be due to the difficulty of measuring separation when there are large oscillations in the velocity while, at the same time, the mean flow velocity is small. The prediction of these points as 0.15 and 0.59 in the DNS of Maass and Schumann [3] is also consistent with the present results.

The shear stress increases rapidly after the minimum value near x/λ=0.40, and has maximum value near x/λ=0.92, which is in agreement with reference data reported in [4]. The shear stress at the upper flat plate wall is computed as 0.0043 in the present work, compared with the value 0.0045 of [4].

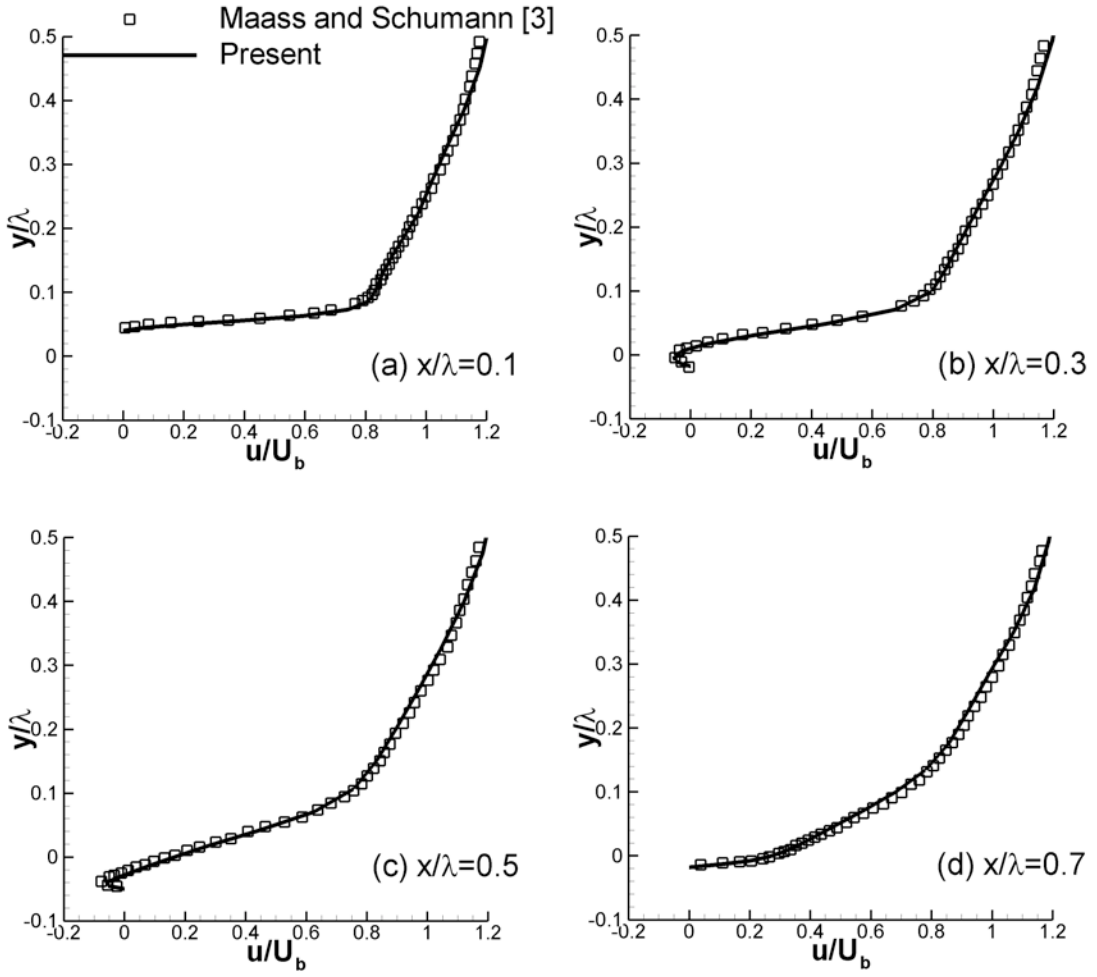

Figure 5. Mean streamwise velocity profiles, (a) x/λ=0.1, (b) x/λ=0.3, (c) x/λ=0.5, (d) x/λ=0.7 (medium mesh case).

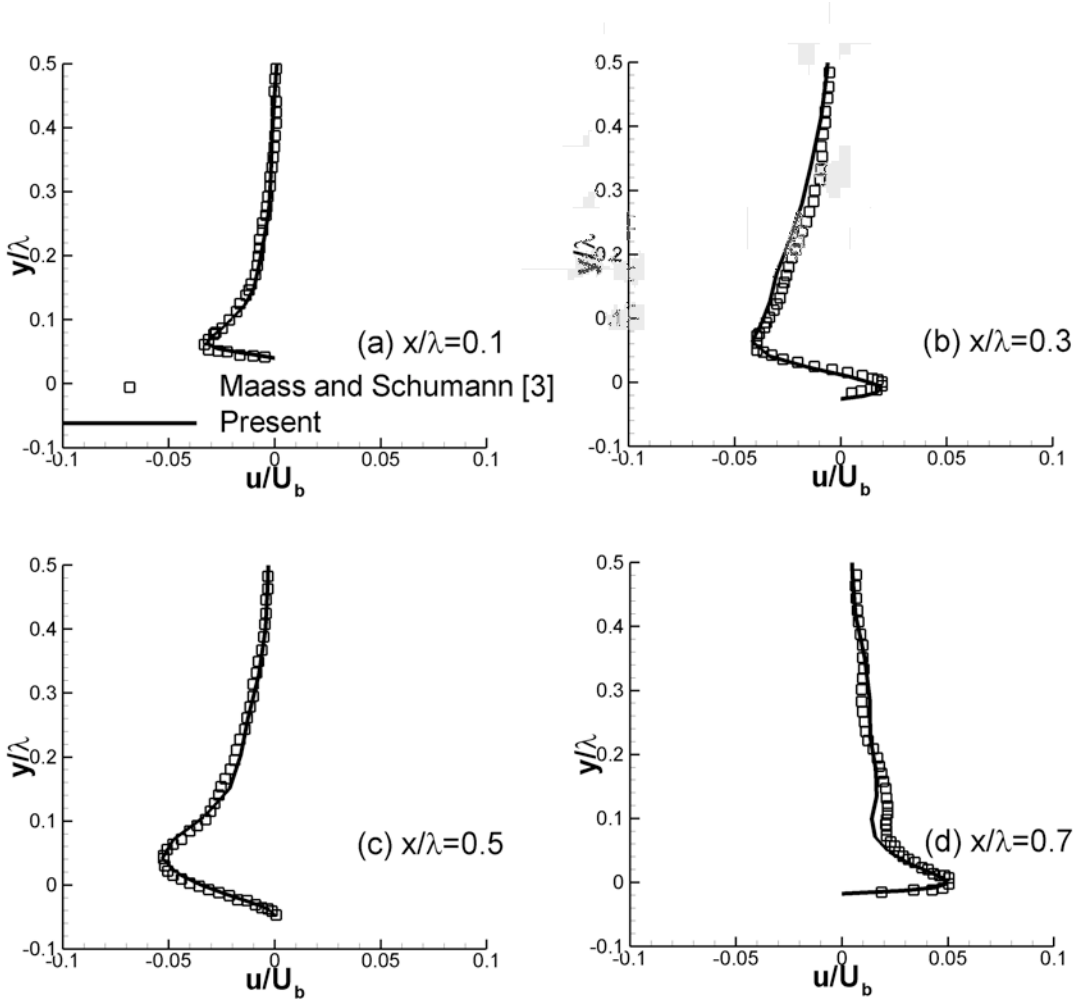

Figure 6. Mean vertical velocity profiles, (a) x/λ=0.1, (b) x/λ=0.3, (c) x/λ=0.5, (d) x/λ=0.7 (medium mesh case).

Figures 5 and 6 show the streamwise and vertical mean velocity profiles at different streamwise locations (x/λ=0.1, 0.3, 0.5, 0.7) and these are compared with the DNS results [3]. Point **a** (x/λ=0.1) is located near the crest of the wavy wall and before the separation point of the flow. Points **b** and **c** (x/λ=0.1, 0.5, respectively) are in the recirculation region. Point **d** (x/λ=0.7) is located after the reattachment point of the flow. The streamwise and vertical velocity profiles agree well with the DNS results reported in [3].

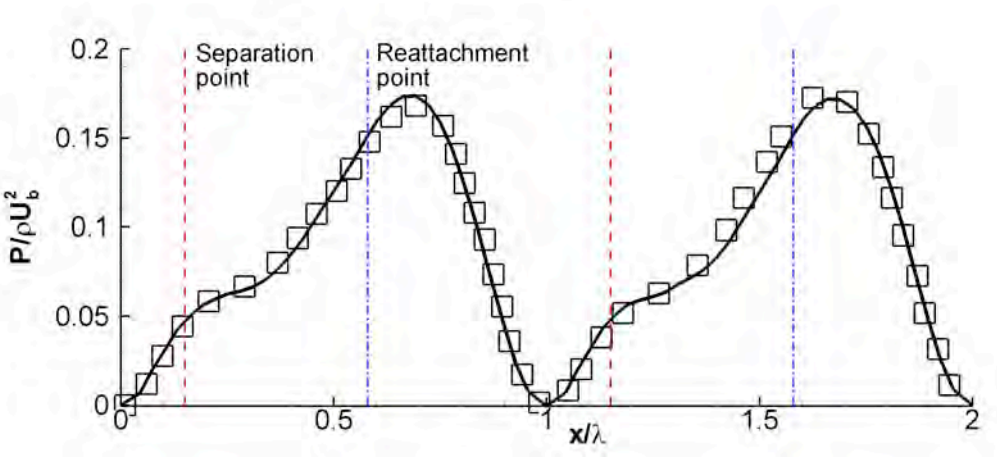

Figure 7. Mean pressure coefficient distribution, line: present simulation, symbol: DNS of Cherukat et al. [4] (medium mesh case).

The mean pressure coefficient along the wavy wall is replotted in Figure 7 along with the locations of separation and reattachment points. The separation bubbles are seen to appear within the adverse pressure gradient regions as is typical. The peak pressure point occurs near x/λ=0.69. From that point onward a favorable pressure gradient dominates until the next crest point at x/λ=1.0.

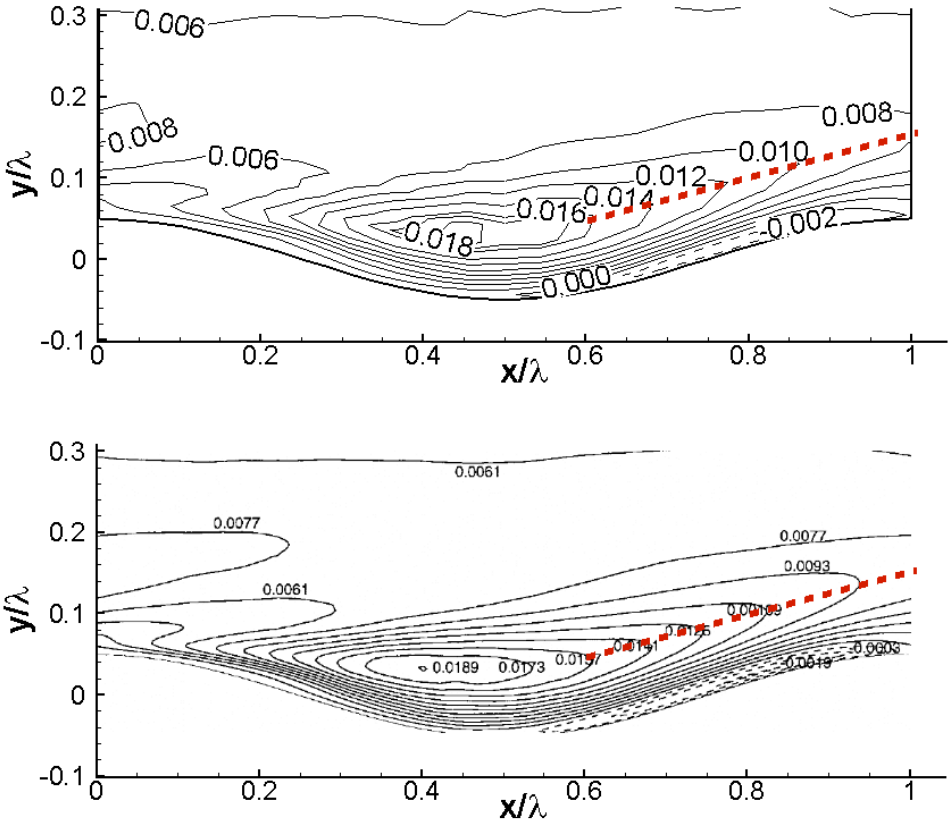

Figure 8. Reynolds stress contours, top: present simulation, bottom: DNS of Cherukat et al. [4] (medium mesh case).

Figure 8 shows the contours of the Reynolds stress term, $-u'v'$. The upper plot displays the present results and the lower one reproduces those of [4]. As shown in Figure 8 (top), the position of maximum Reynolds stress is predicted near the upper region of the trough (x/λ=0.45) and negative values are seen on the windward side near the wall between x/λ=0.53 and 0.99. The DNS results of Cherukat et al. [4] give the maximum value at x/λ=0.40 and the negative region is from x/λ=0.55 to x/λ=1.0. Hudson [1] and others [4, 5] argue that the negative values of Reynolds stress occur due to the calculation of this term in a Cartesian frame rather than in a boundary fitted frame.

Günther and Rohr [2] described these wavy flows in terms of three regions; (I) separation zone, (II) region of local maximum Reynolds stress ($-u'v'$) and (III) region of local minimum Reynolds stress ($-u'v'$). The contours of maximum Reynolds stress after the reattachment point increase in an upward direction, which is represented by the dashed lines in Figure 8. The local maximum in the Reynolds stress contours is approximately located at x=0.08λ above the wall. This coincides with Günther and Rohr's experimental results [2].

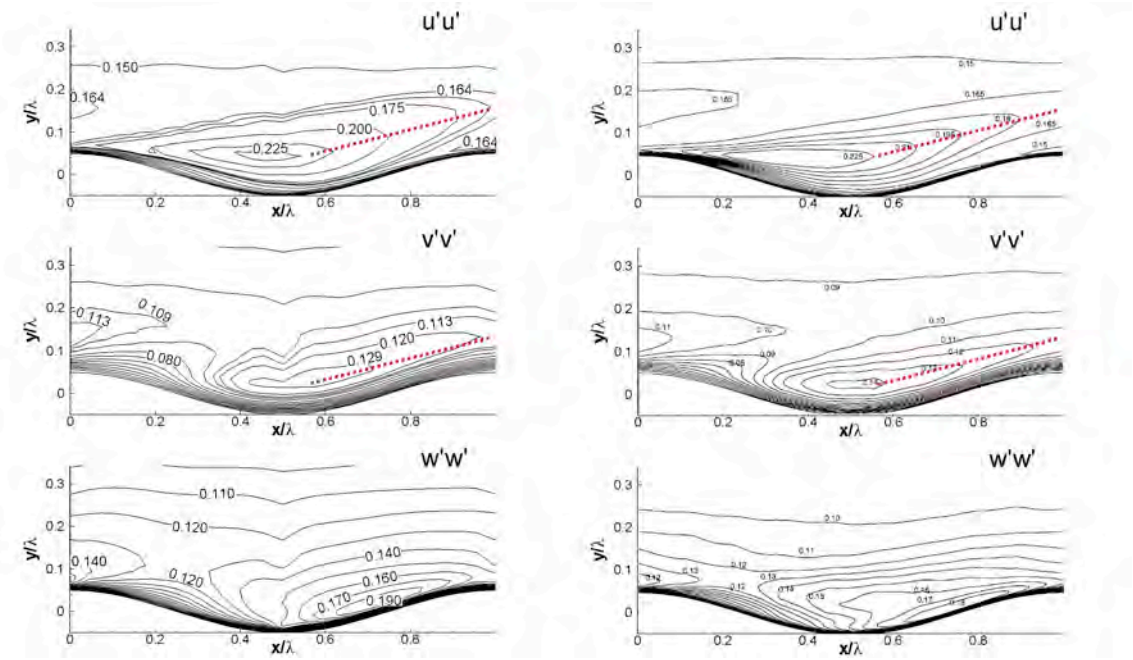

Figure 9. Reynolds stress contours, left: present simulation results, right: DNS of Cherukat et al. [4], top: $u'u'$, middle: $v'v'$, bottom: $w'w'$ (medium mesh case).

The contours of the diagonal components of Reynolds stress are plotted for comparison with DNS results in Figure 9. The locations of maximum streamwise fluctuations are coincident with those of maximum positive Reynolds stress ($-u'v'$). A ridge appears over the crest of the streamwise intensity plot. However, the regions of maximum vertical intensity are closer to the wall than those of the other two variables. Spanwise intensity contours show a different pattern from those of streamwise and vertical intensity. A high intensity region between the trough and the crest indicates that the flow has developed fully three-dimensional structures. These terms contribute to the increase of the turbulent kinetic energy after the reattachment point, as shown in Figure 10.

The profiles of the resolved turbulent kinetic energy at different spanwise locations are shown in Figure 10 and are compared with the DNS results of Maass and Schumann [3]. The present results show very good agreement with the DNS data even though small sharp peaks are apparent at the maximum points of Figures 10(b) and 10(c). The contours of turbulent kinetic energy (not shown here) show the maximum kinetic energy point at x/λ=0.45 which is the same as the DNS results reported in [3].

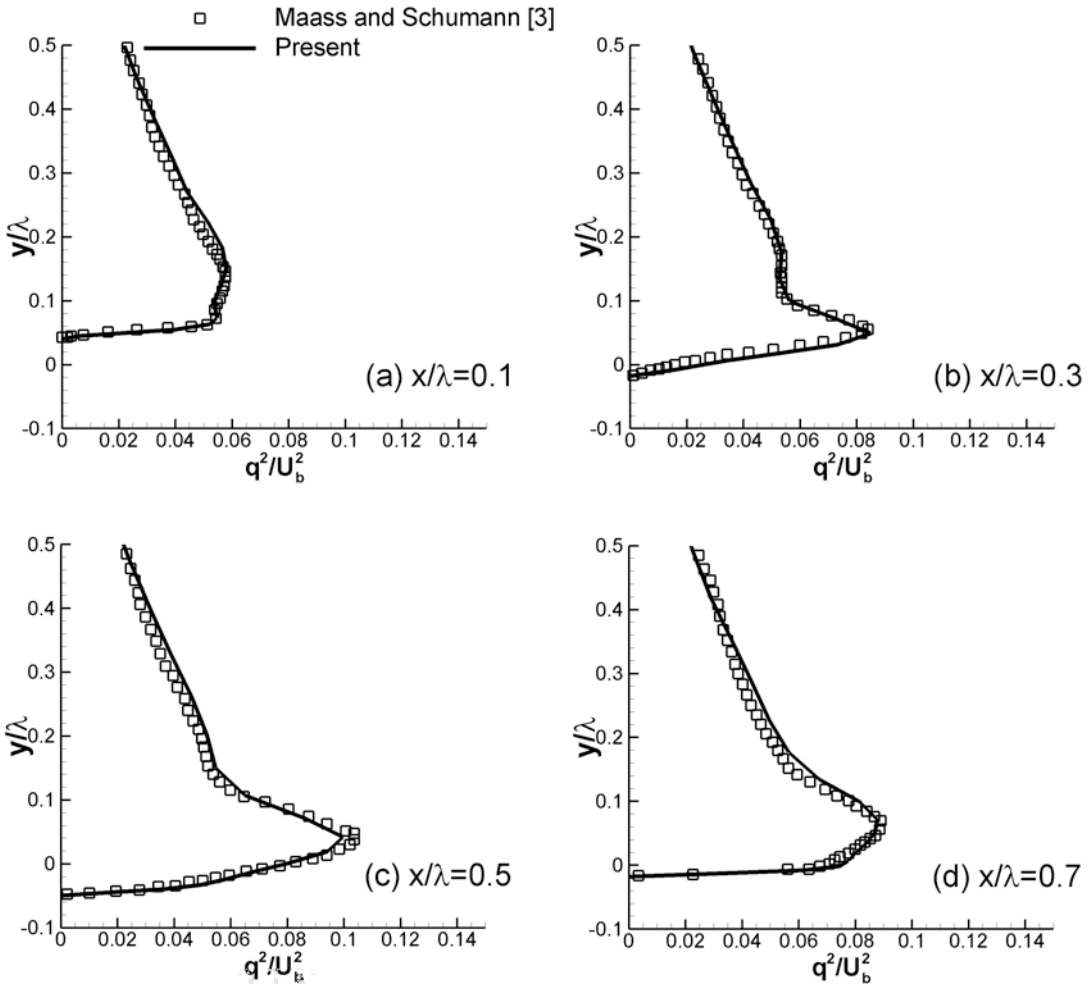

Figure 10 Turbulent kinetic energy profiles, (a) x/λ=0.1, (b) x/λ=0.3, (c) x/λ=0.5, (d) x/λ=0.7 (medium mesh case).

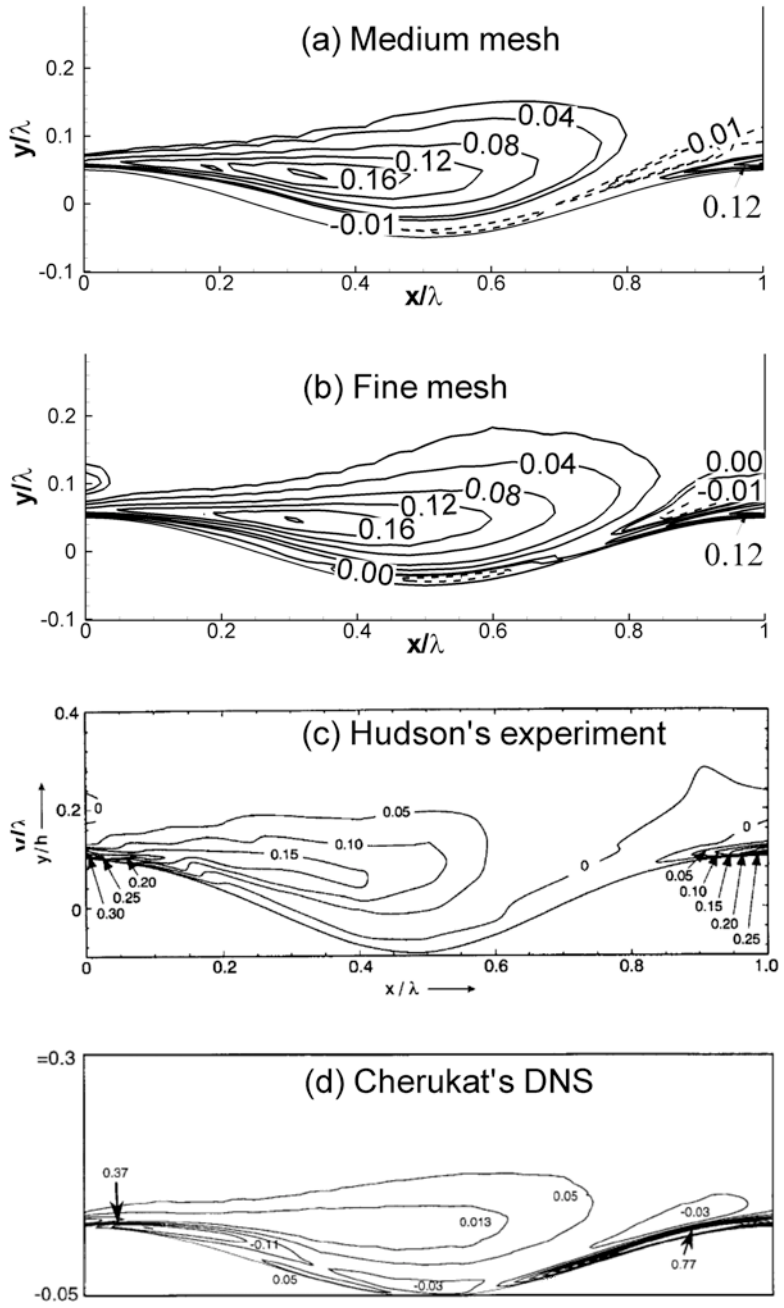

Figure 11. Turbulence production contours, (a) results for the medium mesh, (b) results for the fine mesh, (c) experiment of Hudson et al.[1], (d) DNS of Cherukat et al. [4].

The contours of the production of turbulent kinetic energy ($P_k = -u_i' u_j' \frac{\partial \overline{u_i}}{\partial x_j}$) are shown in Figure 11. The overall patterns displayed by the present simulations are in reasonable agreement with the reference data. Regions where negative production occurs are predicted near the bottom wall, above the high intensity region, between the reattachment point and the next crest. These negative production regions are associated with energy backscatter, that is, transfer of energy from the smaller flow

scales to the larger ones.

The regions of high kinetic-energy production show slightly different patterns in Hudson's experiment [1] and in Cherukat et al. DNS [4]. Hudson's experiment predicts this region near the crest, while numerical simulations of Cherukat et al. show the high intensity region located after the reattachment point to the next crest. Cherukat et al. posited this difference may be caused by improper resolution of Hudson's experiment near the wall in the recirculation zone, which decreases the accuracy of the calculated velocity gradient used in the computation of the production terms from the experimental data. The patterns of high value in this region in the present calculations are qualitatively consistent with the DNS results. Angelis et al. [18] explain the importance of the gradient of spanwise velocity in wavy wall flows and, in particular, near the wall to accurately predict the turbulent kinetic energy production in the flow. This is evident when comparing medium and fine meshes in Figures 11(a) and 11(b). In the medium resolution mesh simulation, the high intensity region is located near the crest of the wavy wall ($x/\lambda \geq 0.85$), while, in the fine mesh simulation, the high intensity region is located toward the reattachment point ($x/\lambda \geq 0.75$) and is spread more widely than for the medium mesh.

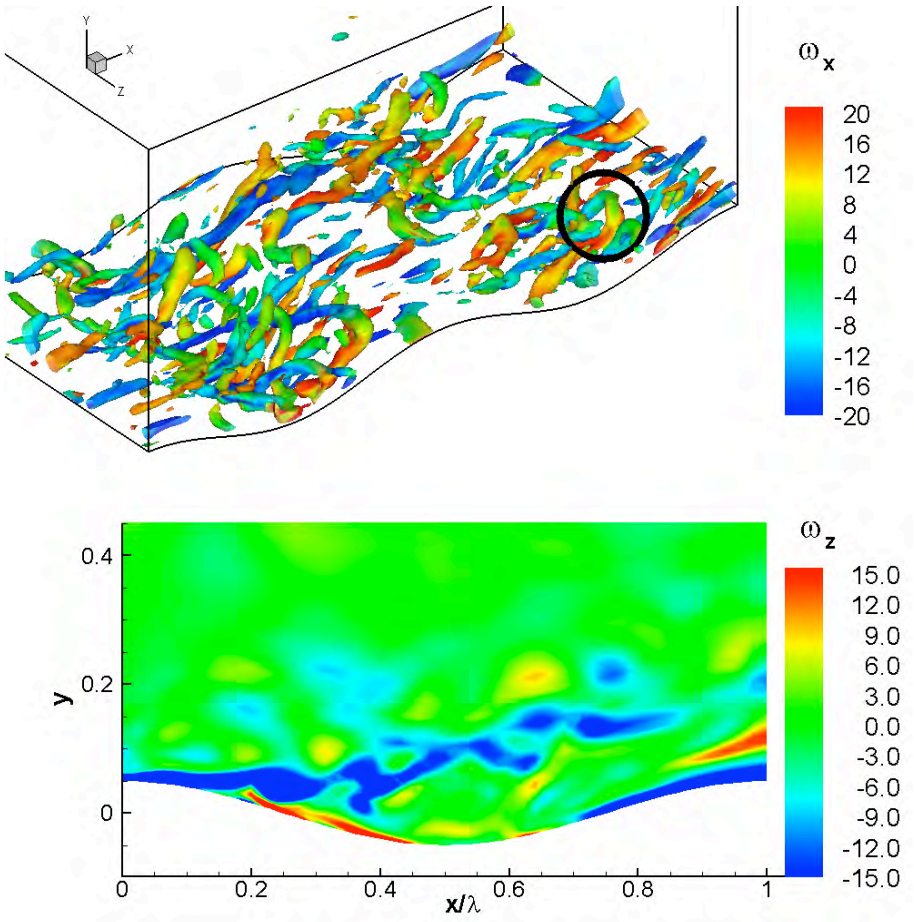

Figure 12. (Top) Isosurfaces of coherent structures at instantaneous time (Q-criterion) of fine mesh, contoured by streamwise vorticity (ω_x), (Bottom) Spanwise vorticity contours in x-y plane at z/λ=0.5.

To study the coherent structures of this fully turbulent flow, the second invariant of the velocity gradient tensor, Q-criterion [19], is calculated for the fine mesh simulation. Even though the predictions of the mean and turbulent statistics for the medium mesh are in excellent agreement with the benchmark experimental and simulated data, the medium mesh resolution is not able to accurately resolve the turbulent coherent structures. Figure 12 (Top) shows the instantaneous vortical structures represented by the isosurfaces of the Q-criterion [19] which are colored with the values of streamwise vorticity (ω_x). Figure 12 shows that the dominant structures are streamwise vortices; some structures begin after the trough and extend to the next crest or trough, while others are generated in the region between the reattachment point and the next crest. These structures appear to scale like the wavelength of the sinusoidal wavy wall. Hairpin vortices are found near the reattachment region and, at this instant, one is marked by a circle in Figure 12 (Top). Vortices aligned with the spanwise direction are rarely found due to the dominant streamwise convection of vortices. Figure 12 (Bottom) shows the contours of the spanwise vorticity (ω_z) in the midsection (z/λ=0.5) of the spanwise direction. High vorticity is generated by the shear layer interaction with the recirculating flow. This high vorticity moves toward the next crest while breaking up. A thin vortex sheet is developed near the wall after the reattachment point and results in the shear layer at the next crest. These observations are consistent with those of other numerical simulations [18, 20].

5. Conclusions

Fully developed turbulent flows with wavy walls are simulated using an isogeometric residual-based variational multiscale method. C^1 quadratic B-spline basis functions are used to solve the incompressible Navier-Stokes equations and represent the geometry. To assess the predictive capabilities of the VMS modeling framework, mean and turbulent statistics as well as instantaneous flow features are compared with the DNS results of Maass and Schumann[3], Cherukat et al. [4] and experimental data of Hudson et al. [1].

Mean velocity and pressure fields show good agreement with DNS results. Turbulent statistics at the wall, such as wall shear stress and pressure coefficient, are in good agreement with reference data. The separation point is predicted at x/λ=0.15 and the reattachment point at x/λ=0.58, in good agreement with the estimation of the size of the recirculation bubble reported in the literature [4].

Overall, the patterns of the contours of the kinetic-energy production are consistent with the DNS results. Additionally, energy backscatter is correctly predicted. As the mesh is refined, particularly in the spanwise direction, the region of higher intensity of production spreads toward the downwind side of the wavy wall, confirming the observation of Angelis et al. [18] that the gradient resolution in the spanwise direction has an important effect on the calculation of production of the turbulent kinetic energy.

Streamwise vortical structures with a length scales comparable to that of the bottom wall wave length are observed as dominant structures in this flow. Hairpin structures are also found in this flow regime. Strong interaction between the shear layer and the recirculation bubble appears to distort the thin boundary layer developing from the previous reattachment point.

From the engineering point of view, the residual-based variational multiscale modeling framework is consistently able to accurately predict the important features of the mean flow as well as those of the turbulent statistics. This observation has been verified herein for separated turbulent flow with relatively coarse meshes. Most statistical quantities for the medium mesh are in excellent agreement with DNS data, but with a reduction of degrees of freedom by at least an order of magnitude. As the mesh is refined, the variational multiscale results converge to those of DNS results, as anticipated from the structures of the variational multiscale modeling theory.

Acknowledgement

This research was supported by the WCU (World Class University) project through the National Research Foundation (R33-10150) and by the Mid-career Researcher Program, NRF grant (2010-0027790), funded by the Korean Government (MEST). T.J.R. Hughes was partially supported by the Office of Naval Research under Contract No. N00014-08-0992, the Development of Energy [National Nuclear Security Administration] under Award No. DE-FC52-08NA28615, and SINTEF under Contract No. UTA10-000374.

References

[1] J.D. Hudson, L. Dykhno and T.J. Hanratty, Turbulence production in flow over a wavy wall, *Experiments in Fluids*, 20, (1996), 257-265.

[2] A. Günther and P.R. von Rohr, Large-scale structures in a developed flow over a wavy wall, *Journal of Fluid Mechanics*, 478, (2003), 257-285.

[3] C. Maass and U. Schumann, Direct numerical simulation of separated turbulent flow over a wavy boundary, in *Flow Simulation with High Performance Computers*, edited by E.H.Hirschel, Notes on Numerical Fluid Mechanics, 52, (1996), 227-241.

[4] P. Cherukat, Y. Na, and T.J. Hanratty, Direct numerical simulations of a fully developed turbulent flow over a wavy wall, *Theoretical and Computational Fluid Dynamics,* 11, (1998), 109-134.

[5] H.S. Yoon, O.A. El-Samni, A.T. Huynh, H.H. Chun, H.J. Kim, A.H. Pham and I.R. Park, Effect of wave amplitude on turbulent flow in a wavy channel by direct numerical simulation, *Ocean Engineering*, 36, (2009), 697-707.

[6] T.S. Park, H.S. Choi, K. Suzuki, Nonlinear model and its application to the flow and heat transfer in a channel having one undulant wall, *International Journal of Heat and Mass Transfer*, 47, (2004), 2403-2415.

[7] Y. Bazilevs, V.M. Calo, J.A. Cottrell, T.J.R. Hughes, A. Reali, G. Scovazzi, Variational multiscale residual-based turbulence modeling for large eddy simulation of incompressible flows, *Computer Methods in Applied Mechanics and Engineering*, 197, (2007), 173-201.

[8] T.J.R. Hughes, V.M. Calo, and G. Scovazzi, Variational and multiscale methods in turbulence, *Mechanics of the 21st Century*, Springer, Dordrecht, The Netherlands, (2005), 153-163.

[9] V.M. Calo, Residual-based multiscale turbulence modeling : finite volume simulations of bypass transition, Ph.D. Thesis, Civil and Environmental Engineering Department, Stanford University. Available at : http://www.ices.utexas.edu/~victor/Calo_Victor_ Thesis.pdf, 2004.

[10] I. Akkerman, Y. Bazilevs, V.M. Calo, T.J.R. Hughes, and S. Hulshoff, The role of continuity in residual-based variational multiscale modeling of turbulence, *Computational Mechanics*, 41, (2008), 371-378.

[11] I. Akkerman, Y. Bazilevs, C.E. Kees, M.W. Farthing, Isogeometric analysis of free-surface flow, *Journal of Computational Physics*, 230, (2011), 4137-4152.

[12] Y. Bazilevs, I. Akkerman, Large eddy simulation of turbulent Taylor-Couette flow using isogeometric analysis and the residual-based variational method, *Journal of Computational Physics*, 229, (2010), 3402-3414.

[13] Y. Bazilevs, C. Michler, V.M. Calo, and T.J.R. Hughes, Isogeometric variational multiscale modeling of wall-bounded turbulent flows with weakly enforced boundary conditions on unstretched meshes, *Computer Methods in Applied Mechanics and Engineering*, 199, (2010), 780-790.

[14] K.E. Jansen, S.S. Collis, C.H. Whiting and F. Shakib, A better consistency for low-order stabilized finite element methods, *Computer Methods in Applied Mechanics and Engineering*, 190, (1999), 305-319.

[15] J.A. Cottrell, T.J.R. Hughes and Y. Bazilevs, Isogeometric analysis: Toward integration of CAD and FEA, Wiley, 2009.

[16] L. Pigel, W. Tiller, The NURBS Book (Monographs in Visual Communication), 2nd ed., *Springer-Verlag, New York*, 1997.

[17] D.F. Rogers, An Introduction to NURBS with Historical Perspective, Academic Press, San Diego, CA, 2001.

[18] V. De Angelis, P. Lombardi, and S. Banerjee, Direct numerical simulation of turbulent flow over a wavy wall, *Physics of Fluids*, 9, (1997), 2429-2442.

[19] Y. Dubief and F. Delcayre, On coherent-vortex indentification in turbulence, *Journal of Turbulence*, 1, (2000), 1-20.

[20] E. Balaras, Modeling complex boundaries using an external force field on fixed Cartesian grids in large-eddy simulations, *Computers & Fluids*, 33, (2004), 375-404.